New Journal of Physics
The open access journal at the forefront of physics

Deutsche Physikalische Gesellschaft DPG
IOP Institute of Physics

Published in partnership with: Deutsche Physikalische Gesellschaft and the Institute of Physics

OPEN ACCESS

RECEIVED
19 February 2022

REVISED
14 August 2022

ACCEPTED FOR PUBLICATION
22 August 2022

PUBLISHED
7 September 2022

PAPER

Anisotropic mode excitations and enhanced quantum interference in quantum emitter-metasurface coupled systems

Wei Fang[1,2,*], Ying Chen[1], Yali Zeng[3], Congjie Ou[1], Gao-xiang Li[4] and Yaping Yang[2,*]

[1] Institute of Systems Science and Department of Physics, College of Information Science and Engineering, Huaqiao University, Xiamen, People's Republic of China
[2] MOE Key Laboratory of Advanced Micro-Structure Materials, School of Physics Science and Engineering, Tongji University, Shanghai, People's Republic of China
[3] Department of Physics and Institute of Electromagnetics of Acoustics, Xiamen University, Xiamen, People's Republic of China
[4] Department of Physics, Huazhong Normal University, Wuhan, People's Republic of China
[*] Authors to whom any correspondence should be addressed.

E-mail: wei_fang@hqu.edu.cn and yang_yaping@tongji.edu.cn

Keywords: quantum interference, surface plasmon modes, quantum emitter, anisotropic metasurfaces

Abstract

This study proposes a nanophotonic structure that supports quantum interference (QI) between orthogonal decay channels in multilevel quantum emitters within the framework of the quantum master equation. The Green functions of the electric field are obtained by applying boundary conditions in the presence of two-dimensional metasurfaces. We demonstrate distinct in-plane excitation features of the surface plasmon modes (SPMs) with the anisotropic metasurfaces tailored to conductivity components. In particular, we observed that the Purcell factor of transitions with orthogonal polarizations experiences unequal enhancements, owing to the anisotropic propagation of the SPMs. This property depends only on the anisotropy of the metasurfaces; thus, it is easily manipulated. Using this platform and considering experimentally achievable material parameters, we predict a strong interference effect in three-level quantum emitters. In principle, this enables the generation of maximum QI. Our study provides a method for realizing QI systems and has potential applications in highly integrated, tuneable quantum devices.

1. Introduction

Tailoring photonics for monolithic integration enables the fabrication and control of electronic-photonic systems at the nanoscale [1–3]. In the last decade, light–matter interaction has been widely studied in two-dimensional layered structures [4]. Generally, most of these structures support the excitation of surface plasmons that exhibit small propagation losses and large field confinements [5, 6]. It has been reported that the hybrid polariton modes of isotropic graphene sheets are electrically [7] or chemically [8] tuneable, which have recently gained significant research attention in application fields such as plasmonic waveguides [9], tuneable terahertz platforms [10], and photodetectors [11]. Motivated by these intriguing features, many studies focus on the manipulation of polariton modes. Among them, two-dimensional anisotropic metasurfaces (TDAMs), such as graphene nanoribbons [12], black phosphorus [13, 14], van der Waals materials [15], and structures based on lithography and etching technologies [16, 17], are promising candidates for integrated quantum photonics devices because their optical responses can easily be manipulated in the laboratory. Owing to the peculiar optical properties of the above TDAMs, they have found applications in hyperlensing [18], cloaking [19], on-chip light manipulation [20], near-field radiative heat transfer [21], biosensors for molecule and virus detection [22], polariton lasing [23], optoelectronics [24], and electro-optic modulators [25].

In the quantum scheme, the spontaneous emission of individual atoms [26] via vacuum modes can occur due to vacuum fluctuations. Purcell proposed that the lifetime of quantum emitters (QEs) placed in a cavity generally suffers strong modifications [27]. More recently, various types of optical structures have

been designed to control the spontaneous decay property of QEs, including metamaterials [28–31], waveguides or cavities [32–36], photonic crystals [37–39], and nanostructures [40–42]. This new paradigm unites quantum optics and nanophotonics, thereby yielding a plethora of applications, such as superradiance [43], squeezing in resonance fluorescence [44], indistinguishable single-photon generation [45], and entanglement enhancement in the quantum field [46]. It has been noted that an anisotropic photonic environment is a key requirement to produce a significant quantum coherence and interference effect in three-level QEs [47]. Agarwal theoretically predicted the QI between the orthogonal transition channels of a V-type Zeeman atom in a cavity formed by conducting plates [48], where the near-degenerate atomic transitions become (anti)parallel in the strong QI regime. This mechanism leads to many optical phenomena, such as lasing without inversion [49], protecting quantum entanglement [50], electro magnetically induced transparency [51, 52], atomic location [53, 54], and spontaneous emission cancellation [55]. Moreover, effective control of the QI effect has been demonstrated by coupling QEs to bulk metamaterials [56], metallic nanostructures [57], and periodic waveguide structures [58]. Compared with the structures mentioned above, TDAMs facilitate an atomic-scale thickness and high tuneability [59, 60]; thus, they possess unique capabilities to control light–matter interactions [61, 62]. Although still in the early stage, they have been extensively employed in the emerging field of quantum photonics [63]. In a recent study, Jha *et al* investigated the QI effect supported by metasurfaces made of subwavelength-scale nanoantennas [64]. The results indicated that polarization-dependent phase shifts of different decay channels can be realized by reasonably designing the dimensions of the nanoantennas. Consequently, the metasurface creates an anisotropic quantum vacuum and enables prominent QI in orthogonal levels of QEs placed in the far-field region.

In this study, we propose a new interference mechanism in hybrid exciton–plasmon systems composed of a V-type three-level QE and TDAM, where the formation of an anisotropic photonic environment strongly relies on the excitation feature of the SPM. For real materials, both the dispersion and propagation properties of the SPM [15, 65] are easily controlled by manipulating the optical response of the metasurfaces. Here, we use a quantum-mechanical formalism for the electromagnetic field excitations [42]. Within this quantization scheme, the excitation features of the SPM and the spontaneous decay rates of the QE in the proximity of the metasurface can be numerically evaluated using the Green function method. We demonstrate the possibility of realizing anisotropic field excitations in the near-field region according to numerical and simulation results. Unequal transition-rate enhancements in orthogonal channels are illustrated depending on the dipole orientation with respect to the crystallographic axes. Consequently, we show that the anisotropic Purcell effect is highly tuneable by engineering the anisotropy of the metasurfaces. When the isofrequency contour exhibits extremely flattened patterns, the anisotropic Purcell effect becomes particularly prominent. Finally, we investigate the influence of material anisotropy on QI strength in orthogonal decay channels of the three-level QE. We demonstrate the tuneability of the QI effect in the proposed systems and predict the generation of maximum QI under particular conditions.

The remainder of this paper is organized as follows. In section 2, we derive the dispersion relation of the SPM and numerically investigate the isofrequency contours. The simulation used to verify the accuracy of the numerical results is also described. In section 3, the Purcell factors with respect to the orthogonal in-plane transitions are investigated following the proper quantization scheme. Finally, we analyse the influence of surface anisotropy on the QI strength. Additionally, we consider real two-dimensional surfaces and discuss the experimental implementation of the proposed system. The conclusions are drawn in section 4. The appendices provide further details of the analyses presented in sections 2 and 3.

2. Mode excitations of the in-plane SPM for different surface topologies

We begin by considering the case of a linear polarized current dipole located in the upper half space of an infinitesimally thin, free-standing TDAM (with host medium dielectric permittivity and permeability equal to the vacuum values), which has a conductivity tensor that can be defined as

$$\bar{\boldsymbol{\sigma}} = \begin{pmatrix} \sigma_{xx} & 0 \\ 0 & \sigma_{yy} \end{pmatrix}. \tag{1}$$

In the case of isotropic surfaces, either transverse-magnetic (TM) or transverse-electric (TE) SPMs can be supported [66]; however, in the anisotropic case, both the TM- and TE-polarized SPMs can be supported simultaneously [17]. Moreover, in the near-field region, the spontaneous decay of QEs is primarily determined by the excitation features of the SPM. We inspect the plasmon dispersion relation to understand the behaviour of the SPM. Following the method mentioned in reference [67], the scattered Green functions are derived by introducing the electric Hertzian potential and imposing boundary conditions

(see appendix A for more details). By determining the zero(s) of the denominator in the Green functions arising from equations (A.21)–(A.24), we obtain the dispersion relation satisfying

$$\frac{k_x^2}{\sigma_{yy}} + \frac{k_y^2}{\sigma_{xx}} = \frac{1}{\sigma_{xx}\sigma_{yy}}\left[k_1^2(\sigma_{xx}+\sigma_{yy}) + 2\omega\beta_1\left(\varepsilon_1 + \frac{\mu_1}{4}\sigma_{xx}\sigma_{yy}\right)\right], \tag{2}$$

where ω is the frequency of the current dipole, ε_1 and μ_1 are vacuum permittivity and permeability, $k_1 = \omega/c$ denotes the vacuum wave number, and $\beta_1 = \sqrt{k_1^2 - k^2}$ represents the vertical component of the wave number in the source region. It is clear that the solution of equation (2) defines the wave front propagation of the SPM supported by the TDAM. However, in the anisotropic case, the wave front and propagation direction do not coincide. Instead, the energy-propagation direction of the SPM is typically defined by the group velocity $\nabla_{\mathbf{k}}\omega(\mathbf{k})$, where $\mathbf{k} = k_x\mathbf{e}_x + k_y\mathbf{e}_y$ ($\mathbf{e}_x$ and $\mathbf{e}_y$ are unit vectors along the x and y directions) describes the in-plane wave vector [68]. As demonstrated by equation (2), an analytical expression of the group velocity is not available, owing to the complicated dispersion relation. However, the definition of the group velocity indicates that the energy-propagation direction of the surface modes must be orthogonal to the isofrequency contours.

However, the dispersion relation actually predicts different topologies for the SPM tailored to the conductivity components. The elliptic topology arises when both the diagonal components of the conductivity tensor have the same signs in their imaginary parts, i.e., for $\mathrm{Im}[\sigma_{xx}], \mathrm{Im}[\sigma_{yy}] > 0$ or $\mathrm{Im}[\sigma_{xx}], \mathrm{Im}[\sigma_{yy}] < 0$. However, in the latter case, the surfaces can only support the excitation of TE-polarized SPM, thereby leading to a poor field confinement, which is of little practical interest to the topic of enhanced light–matter interactions. The hyperbolic topology arises when the TDAM becomes capacitive along one optical axis and inductive along the orthogonal one, which requires that the imaginary parts of the conductivity components satisfy the relation $\mathrm{Im}[\sigma_{xx}] \cdot \mathrm{Im}[\sigma_{yy}] < 0$. In this case, both the TE- and TM-polarized SPMs can be simultaneously supported by the surfaces. As we will discuss later in this section, the dispersion topologies for the SPM are primarily affected by the optical response of the surfaces. Under particular conditions, manipulation of the surface conductivities results in anisotropic mode excitations, dipole radiations, and QI enhancement.

To unveil the mechanisms behind the light–matter interaction mediated by the TDAM, we start by investigating the isofrequency contours for different surface topologies. Figures 1(a) and (b) illustrate the isofrequency contours in the elliptic dispersion case, for which the metasurfaces support only the TM-polarized SPM because the imaginary part of the conductivities is positive. It is clear that when one of them becomes much larger, for example, $\sigma_{xx}^i \gg \sigma_{yy}^i$, the k surface exhibits a quasielliptic form that is elongated along the direction of the smaller conductivity component. This property is well illustrated by the red solid and green dashed curves, where the flattening of the k surface depends on the ratio of the imaginary parts between the diagonal components of the conductivity tensor.

It should be noted that the wave number of the supported SPM decreases owing to the increase in the optical response (the absolute values of the imaginary part of the conductivity components) of the metasurfaces. This is primarily due to the decrease in the field confinement of the SPM. Moreover, according to the dispersion relation described by equation (2), the branch points related to the different propagating plasmonic modes in the k_x plane with TM and TE polarizations (denoted by the superscripts p and s) are $k_y^p = k_1\sqrt{1 - 4\varepsilon_1/\mu_1\sigma_{yy}^2}$ and $k_y^s = k_1\sqrt{1 - \mu_1\sigma_{xx}^2/4\varepsilon_1}$, respectively. These expressions clearly imply that with an increase in the conductivity components, the wave number of the TM surface modes gradually decreases to the vacuum value k_1; thus, the field becomes poorly confined near the metasurface.

Figures 1(c) and (d) show the isofrequency contours in the hyperbolic regime. Here, only the case of $\sigma_{xx}^i < 0, \sigma_{yy}^i > 0$ is considered, and the results are easily extended to another hyperbolic case with conductivity components that satisfy $\sigma_{xx}^i > 0, \sigma_{yy}^i < 0$. In contrast to the previous case, the isofrequency contour of the SPMs forms hyperbolas with larger wave numbers. With the assumption of large in-plane wave number for the excited SPM ($k_x, k_y \gg k_1$), the solutions of equation (2) can be approximated as $k_y = \pm k_x\sqrt{|\sigma_{xx}^i|/|\sigma_{yy}^i|}$, which indicate the plasmons with wave vectors on hyperbola asymptotes. This description implies narrow beams of the SPM carrying energy along the directions normal to the hyperbolas. In agreement with the qualitative analysis presented in figure 1(c), the surface anisotropy significantly modifies the energy flow of the hyperbolic plasmons.

As mentioned previously, hyperbolic metasurfaces support the simultaneous excitation of the TM and TE plasmon modes. The inset of figure 1(d) shows that the phase transition between these two critical plasmon modes occurs due to the manipulation of surface anisotropy. For small conductivities, the isofrequency contour of the TM modes is represented by hyperbolas, where the dispersion of the TE modes exhibits a close loop in the centre (orange dashed-dotted line in the inset). In this case, the TE modes are poorly confined near the metasurfaces. The circumstance changes considerably for large conductivities,

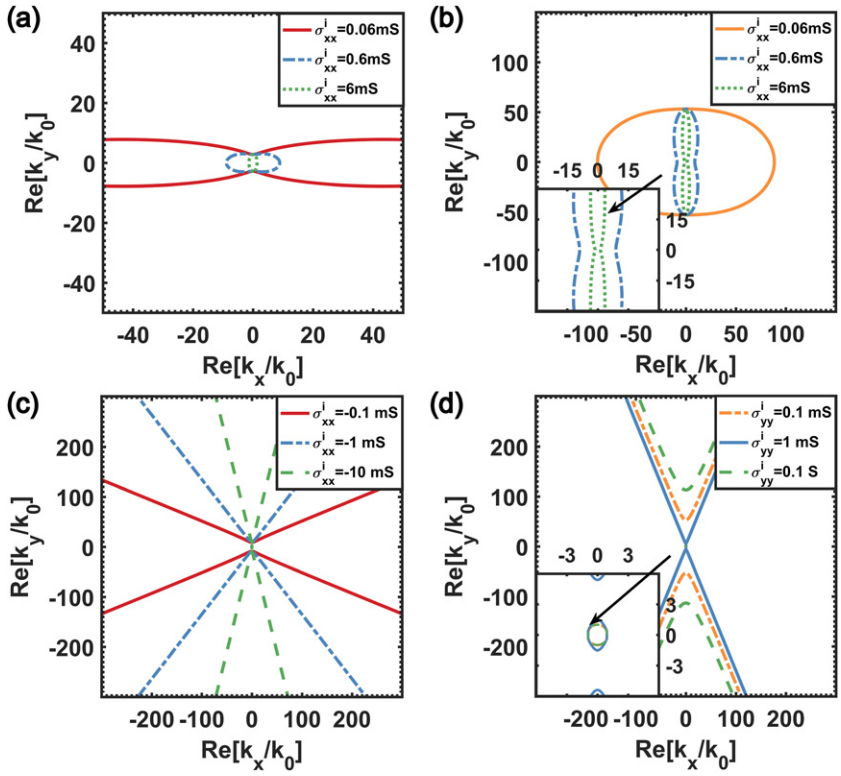

Figure 1. Isofrequency contours of the SPM supported by the TDAM under different conditions. Elliptic topology: (a) $\sigma_{xx} = 0.001 + \sigma^i_{xx}$i mS, $\sigma_{yy} = 0.001 + 2$i mS and (b) $\sigma_{xx} = 0.001 + \sigma^i_{xx}$i mS, $\sigma_{yy} = 0.001 + 0.1$i mS. Hyperbolic topology: (c) $\sigma_{xx} = 0.001 + \sigma^i_{xx}$i mS, $\sigma_{yy} = 0.001 + 0.6$i mS and (d) $\sigma_{xx} = 0.001 - 6\sigma^i_{yy}$i mS, $\sigma_{yy} = 0.001 + \sigma^i_{yy}$i mS.

where the dispersion of the TE modes exhibits hyperbolas (green dashed line in the figure), and the TM modes become poorly confined. In general, the hyperbolic metasurfaces can support a large amount of the overall local density of states compared with the elliptic case, owing to the dominant excitation of either the TM or TE plasmon modes.

To better understand the field excitation features, we plot the spatial distribution and dispersion relation of the SPM using the finite element method (COMSOL Multiphysics, COMSOL Inc., Sweden [69]). The model sets a linear current dipole placed above the TDAM at a distance of $L = 10^{-3}\lambda_a$; the operation frequency is fixed at 60 THz. As shown in figure 2(a), in the extremely elliptic case, where the isofrequency contour is elongated along the x optical axis, the energy flow of the SPM can be well guided along particular directions at small angles with respect to the y optical axis. In contrast to the isotropic case, for the metasurfaces considered here, the in-plane anisotropy also induces a dominant difference among the field components. This feature is well illustrated in the insets, which show detailed views of the field amplitudes $\mathbf{E}_x$ and $\mathbf{E}_y$ near the current source. As indicated, the field amplitudes at the position of the current source are $\mathbf{E}^{\mathrm{o}}_x = -1.8 \times 10^{18}$ and $\mathbf{E}^{\mathrm{o}}_y = -2.8 \times 10^{16}$ in units of V m^{-1}. We compare the ratio of the field components $\mathbf{E}^{\mathrm{o}}_x/\mathbf{E}^{\mathrm{o}}_y$ according to the simulation (the approximated value is 64.8) and the numerical results (evaluated using the Green functions in equations (A.20)–(A.29) and the field definitions in equations (A.30)–(A.32); a value of 67.4 is obtained for the case under consideration), and it is clear that our numerical results achieve a high accuracy in describing light–matter interactions. Finally, the FFT of the spatial field distribution is given in figure 2(b). The result is in good agreement with the isofrequency contour obtained via the Green function approach, which is depicted by the red solid line in figure 1(a).

Additional to the material anisotropy, the dipole-metasurface distance also influences the anisotropic excitation of the field amplitudes $\mathbf{E}_x$ and $\mathbf{E}_y$. It can be observed in the inset of figure 2(a) that the ratio of the field components continuously decreases with an increase in distance L, which implies a decline in the coupling strength between the dipole and metasurfaces. Physically, the phenomenon can be understood as follows. For small dipole-metasurface distances, the excitation feature of the dipole field is strongly modified by the optical response of the surfaces. Consequently, prominent discrepancies between the in-plane field amplitudes can be produced, owing to strong excitations of the anisotropic SPM. With a further increase in the distance L, the coupling between the dipole and SPM weakens [70], thereby leading to a sharp decrease in the ratio $\mathbf{E}^{\mathrm{o}}_x/\mathbf{E}^{\mathrm{o}}_y$. This ratio decreases to unity when the distance is sufficiently large,

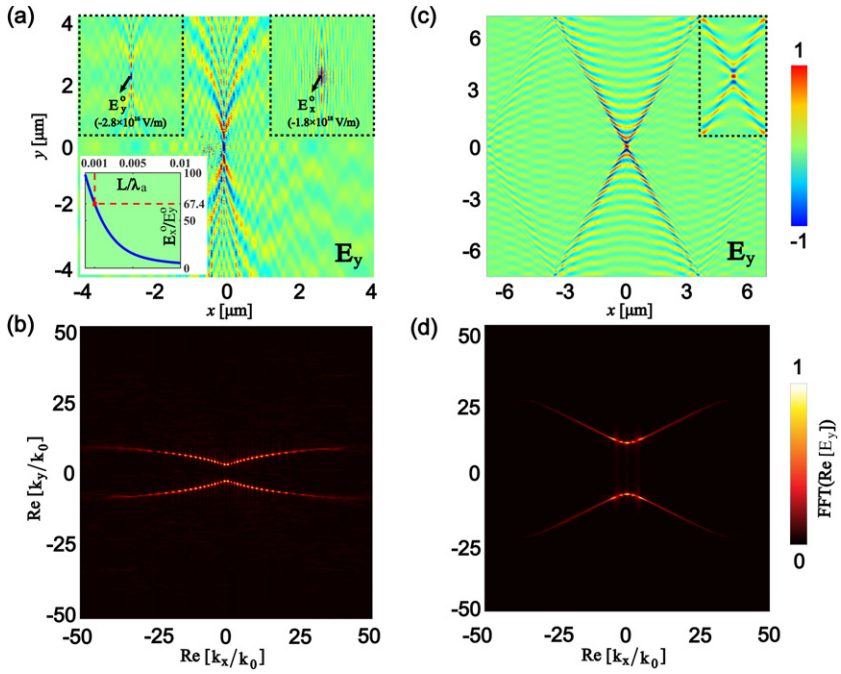

Figure 2. Spatial distribution of the in-plane field amplitudes evaluated in the source plane (subfigures (a) and (c)) and fast Fourier transformation (FFT) of the SPM (subfigures (b) and (d)) excited by current dipoles (with the strength 1 A m) placed above the metasurfaces with a distance of $L = 10^{-3}\lambda_a$ and an operation frequency fixed at 60 THz. (a) Main panel: the field amplitude $\mathbf{E}_y$ in the elliptic dispersion case $\sigma_{xx} = 0.001 + 0.06\mathrm{i}$ mS, $\sigma_{yy} = 0.001 + 2\mathrm{i}$ mS. Inset panels: detailed views of the spatial distributions of the field amplitudes $\mathbf{E}_x^o$ and $\mathbf{E}_y^o$ evaluated at $(0, 0, 10^{-3}\lambda_a)$. The ratio $\mathbf{E}_x^o/\mathbf{E}_y^o$ is also investigated as a function of the distance L. (c) The field amplitude $\mathbf{E}_y$ in the hyperbolic dispersion case: $\sigma_{xx} = 0.001$–$0.1\mathrm{i}$ mS, $\sigma_{yy} = 0.001 + 0.6\mathrm{i}$ mS. The FFT of the spatial field distributions are also plotted in figures (b) and (d) in comparison to the relevant results shown in figures 1(a) and (c).

which indicates an isotropic excitation of the field amplitudes. Notably, for systems that consist of QEs interacting with anisotropic metasurfaces, this behaviour demonstrates that the dipole decouples from the surfaces, and the spontaneous decay only occurs via free vacuum modes.

In figures 2(c) and (d), the spatial distributions and FFT of the excited plasmon field with a hyperbolic dispersion are also investigated. Generally, the unidirectional excitation of the SPM on metasurfaces can be observed, and the radiation energy is channelled along specific directions orthogonal to the hyperbola asymptotes. In figure 2(d), the hyperbolic isofrequency contour can be clearly identified through the FFT of the spatial field, which is in good agreement with the numerical result shown in figure 1(c).

3. Anisotropic Purcell effect and enhanced quantum interference of three-level QEs

Based on the discussions in the previous section, it is clear that TDAMs support the anisotropic excitation of in-plane field amplitudes. In this section, we mainly focus on the quantum interference phenomena of QEs coupled with the TDAM. We consider the case of a three-level QE interacting with the SPM excited on anisotropic metasurfaces, which is illustrated by figure 3. It is probable that dipoles with different in-plane polarizations will display distinct spontaneous decay behaviours, owing to the anisotropic excitations of the SPM. Here, two excited states of the QE are assumed to be close; they are denoted by the states $|1\rangle$ and $|2\rangle$ with energies $\hbar\omega_1$ and $\hbar\omega_2$, respectively, and the energy of the ground state is equal to zero and labelled as $|g\rangle$. In our notation, the dipole moment operator of the QE is denoted by $\boldsymbol{l} = l\big(\hat{\sigma}_1^+\mathbf{e}_- + \hat{\sigma}_2^+\mathbf{e}_+\big) + \mathrm{h.c.}$, with l defining the magnitude of the dipole, and $\mathbf{e}_- = (\mathbf{e}_x - \mathrm{i}\mathbf{e}_y)/\sqrt{2}$ and $\mathbf{e}_+ = (\mathbf{e}_x + \mathrm{i}\mathbf{e}_y)/\sqrt{2}$ refer to the left- and right-rotating unit vectors of the transitions $\hat{\sigma}_1^+ = |1\rangle\langle g|$ and $\hat{\sigma}_2^+ = |2\rangle\langle g|$, respectively. Under the rotating-wave approximation, the Hamiltonian of the system can be written as

$$\hat{H} = \int \mathrm{d}\mathbf{r} \int_0^\infty \mathrm{d}\omega \hbar\omega \hat{\mathbf{f}}^\dagger(\mathbf{r},\omega)\hat{\mathbf{f}}(\mathbf{r},\omega) + \hbar\omega_a(|1\rangle\langle 1| + |2\rangle\langle 2|) - \left[l(\hat{\sigma}_1^+\mathbf{e}_- + \hat{\sigma}_2^+\mathbf{e}_+)\cdot\int_0^\infty \mathrm{d}\omega\hat{\mathbf{E}}^{(+)}(\mathbf{r}_a,\omega) + \mathrm{h.c.}\right]. \quad (3)$$

In equation (3), $\hat{\mathbf{f}}^{\dagger}(\mathbf{r},\omega)$ and $\hat{\mathbf{f}}(\mathbf{r},\omega)$ are the bosonic vector field operators for the elementary excitations of the photonic reservoir in the presence of the TDAM [71], $\omega_1 \approx \omega_2 = \omega_a$ represents the resonance frequency between the two degenerate upper levels and the lower level of the three-level QE, with the energy of the lower level considered zero. The QE is placed at the position $\mathbf{r}_a = (0, 0, 10^{-3}\lambda_a)$, that is, with a distance of $10^{-3}\lambda_a$ above the metasurface. The electric-field vector operator in the frequency domain is as follows [71]:

$$\hat{\mathbf{E}}^{(+)}(\mathbf{r},\omega) = \mathrm{i}\omega\mu_0 \int \mathrm{d}\mathbf{r}'\bar{\mathbf{G}}(\mathbf{r},\mathbf{r}',\omega)\cdot\hat{\mathbf{J}}_n(\mathbf{r}',\omega), \tag{4}$$

where $\bar{\mathbf{G}}(\mathbf{r},\mathbf{r}',\omega)$ is Green's dyadic of the electromagnetic field evaluated at the frequency ω and positions $\mathbf{r}$ and $\mathbf{r}'$. The noise current operator $\hat{\mathbf{J}}_n(\mathbf{r}',\omega)$ takes the form $\hat{\mathbf{J}}_n(\mathbf{r}',\omega) = \omega\sqrt{\hbar\varepsilon_0\,\mathrm{Im}[\varepsilon(\mathbf{r}',\omega)]/\pi}\hat{\mathbf{f}}(\mathbf{r},\omega)$, which acts as the current source of the field and satisfies the following wave equation:

$$\nabla\times\mu^{-1}(\mathbf{r},\omega)\nabla\times\hat{\mathbf{E}}(\mathbf{r},\omega) - \omega^2c^{-2}\varepsilon(\mathbf{r},\omega)\hat{\mathbf{E}}(\mathbf{r},\omega) = \mathrm{i}\omega\mu_0\hat{\mathbf{J}}_n(\mathbf{r},\omega), \tag{5}$$

where $\varepsilon(\mathbf{r},\omega)$ and $\mu(\mathbf{r},\omega)$ are position- and frequency-dependent permittivity and permeability, respectively. At zero temperature, the creation and annihilation field operators satisfy the following commutation relations:

$$[\hat{\mathbf{f}}(\mathbf{r},\omega),\hat{\mathbf{f}}^{\dagger}(\mathbf{r}',\omega')] = \delta(\mathbf{r}-\mathbf{r}')(\omega-\omega'), \tag{6}$$

$$[\hat{\mathbf{f}}(\mathbf{r},\omega),\hat{\mathbf{f}}(\mathbf{r}',\omega')] = 0. \tag{7}$$

Starting from the Hamiltonian given in equation (3) and the quantization scheme described by equations (4)–(7), we transform into the interaction picture and apply second-order perturbation theory. Under the Born–Markovian approximation, the motion equations for the expectation value of the Pauli operators appear to be: [72]

$$\frac{\mathrm{d}}{\mathrm{d}t}\langle\hat{\sigma}_{11}\rangle = -2\gamma_1\langle\hat{\sigma}_{11}\rangle - \kappa_2\big(\langle\hat{\sigma}_{12}\rangle + \langle\hat{\sigma}_{21}\rangle\big), \tag{8}$$

$$\frac{\mathrm{d}}{\mathrm{d}t}\langle\hat{\sigma}_{22}\rangle = -2\gamma_2\langle\hat{\sigma}_{22}\rangle - \kappa_1\big(\langle\hat{\sigma}_{12}\rangle + \langle\hat{\sigma}_{21}\rangle\big), \tag{9}$$

$$\frac{\mathrm{d}}{\mathrm{d}t}\langle\hat{\sigma}_{12}\rangle = -(\gamma_1+\gamma_2)\langle\hat{\sigma}_{12}\rangle - \kappa_1\langle\hat{\sigma}_{11}\rangle - \kappa_2\langle\hat{\sigma}_{22}\rangle, (\hat{\sigma}_{ij} = |i\rangle\langle j|). \tag{10}$$

In the above equations, γ_1 and γ_2 are spontaneous decay coefficients for the transitions $|1\rangle \to |g\rangle$ and $|2\rangle \to |g\rangle$, respectively, which are modified by the photonic reservoir in the presence of a TDAM. κ_1 and κ_2 represent the QI between two decay channels. Clearly, nonvanished coefficients κ_j will produce a QI effect. In this case, the expectation values of the operators $\langle\hat{\sigma}_{11}\rangle$, $\langle\hat{\sigma}_{22}\rangle$, and $\langle\hat{\sigma}_{12}\rangle$ couple with each other during the evolution. The spontaneous decay and QI coefficients can be expressed in forms of the Green functions as follows:

$$\begin{aligned}\gamma_1 = \gamma_2 = \gamma &= \frac{1}{2}\big(\Gamma_x + \Gamma_y\big)\\ &= \frac{l^2\omega_a^2}{\hbar\varepsilon_0c^2}\,\mathrm{Im}\big[\bar{\mathbf{G}}_{xx}(\mathbf{r}_a,\mathbf{r}_a,\omega_a) + \bar{\mathbf{G}}_{yy}(\mathbf{r}_a,\mathbf{r}_a,\omega_a)\big],\end{aligned} \tag{11}$$

and

$$\begin{aligned}\kappa_1 = \kappa_2 = \kappa &= \frac{1}{2}\big(\Gamma_x - \Gamma_y\big)\\ &= \frac{l^2\omega_a^2}{\hbar\varepsilon_0c^2}\,\mathrm{Im}\big[\bar{\mathbf{G}}_{xx}(\mathbf{r}_a,\mathbf{r}_a,\omega_a) - \bar{\mathbf{G}}_{yy}(\mathbf{r}_a,\mathbf{r}_a,\omega_a)\big],\end{aligned} \tag{12}$$

where $\mathrm{Im}[\bar{\mathbf{G}}_{xx(yy)}(\mathbf{r}_a,\mathbf{r}_a,\omega_a)]$ represents the imaginary part of the xx (yy) component of the Green dyadic function, Γ_x and Γ_y denote the spontaneous decay rates of dipole moments with magnitude m and polarizations along two optical axes of the TDAM. It should be noted that in the derivation of equations (11) and (12), the imaginary part of $\bar{\mathbf{G}}_{xy}(\mathbf{r}_a,\mathbf{r}_a,\omega_a)$ has been neglected because it vanishes in the structure under consideration (i.e. for metasurfaces with vanished transverse conductivity, see appendix A for more details). The relative strength p is defined to measure the degree of QI, with the form [73]

$$p = \frac{\kappa}{\sqrt{\gamma_1\gamma_2}} = \frac{\Gamma_x - \Gamma_y}{\Gamma_x + \Gamma_y}. \tag{13}$$

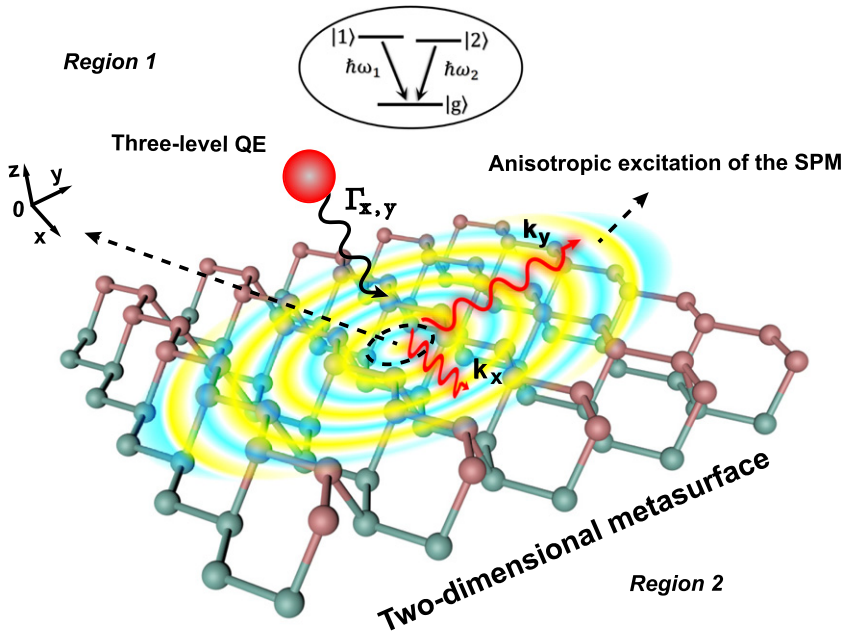

Figure 3. Schematic illustration of a three-level QE coupled with the TDAM via anisotropic SPM; the upper and lower half-space are labelled as region 1 and region 2, respectively.

According to equation (13), it is clear that the QI effect disappears in the case of a three-level QE interacting with s free vacuum or isotropic photonic modes, which can be attributed to the vanishing of κ. As we have previously shown, TDAMs support the anisotropic excitations of the SPM with large field confinement. Moreover, the metasurfaces support the anisotropic excitation of the in-plane field amplitudes. Thus, the production and enhancement of the QI effect is expected if the QE is coupled with the metasurfaces. If the photonic environment near the QE becomes highly anisotropic, such that $\Gamma_{x(y)} \gg \Gamma_{y(x)}$ is satisfied, the transition channels are effectively parallel to each other, and maximum QI with the relative strength $p \approx \pm 1$ can be achieved.

In figure 4, the Purcell factors ($\mathcal{F}_{x(y)} = \Gamma_{x(y)}/\Gamma_0$, which demonstrates the enhancement of the spontaneous decay rate $\Gamma_{x(y)}$ in the presence of TDAM; Γ_0 is the decay rate in the free vacuum) of the in-plane dipoles with orthogonal polarizations and the relative strength of the QI are numerically investigated according to equations (11)–(13) and the Green functions given in the appendix. Notably, for the dipole-metasurface distance under consideration, total coupling between the dipoles and SPM can be realized [70]. As illustrated by figures 4(a) and (b), both the x- and $y-$polarized dipoles display large Purcell factors in the extremely elliptic case (i.e., $\sigma^i_{yy} \gg \sigma^i_{xx}$ or $\sigma^i_{xx} \gg \sigma^i_{yy}$ is satisfied). This can be well understood by combining the results shown in figures 1 and 2. For example, the case of $\sigma^i_{yy} \gg \sigma^i_{xx}$ actually indicates quasielliptic isofrequency contours elongated along the k_x axis (red solid curve in figure 1(a)). Under this circumstance, the energy propagation of the supported SPM primarily distributes in small angles with respect to the y axis (figure 2(a)). As a result, the overall density of states accounting for the spontaneous decay of the $x-$polarized dipole becomes dominant, which leads to a strong enhancement in the anisotropic Purcell effect ($\mathcal{F}_x \gg \mathcal{F}_y$).

Additionally, sharp declines in the Purcell factors can be observed with an increase in surface conductivities. This behaviour mainly originates from the decrease in the wave numbers of the supported SPM for large conductivities. For small wave numbers, the plasmon field is poorly confined and unable to couple energy from the incoming waves with large wave numbers (green dotted curve in figure 1(a)). In the extreme case of $\sigma^i_{xx}, \sigma^i_{yy} \gg \sigma_0$ ($\sigma_0 = e^2/4\hbar$ is the conductance quantum), the TM surface modes are poorly confined near the metasurface; thus, coupling between the QE and SPM is negligible. Instead, the free vacuum modes play a key role in determining the spontaneous decay of the dipoles. Based on the above analysis, maximum QI occurs in the extremely elliptic regimes, which is illustrated by figure 4(c).

To clearly identify the influence of surface topology on the spontaneous decay and QI, we also investigate the Purcell factor and the relative strength of the QI in the hyperbolic regime. As demonstrated in figures 5(a) and (b), the spontaneous decay rate increases considerably compared to the elliptic dispersion case. Combined with the results shown in figure 1, it can be deduced that metasurfaces with a hyperbolic topology support the excitation of the SPM with a larger total density of states, owing to the hyperbola feature of the isofrequency contour.

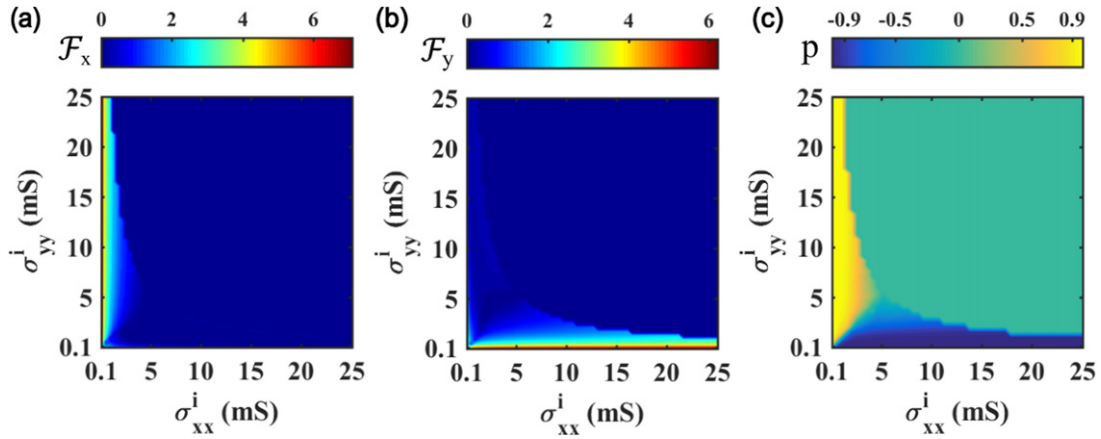

Figure 4. Purcell factors in the logarithmic scale and the relative strength of the QI; both are functions of the surface conductivities ($\sigma_{xx(yy)} = 0.001 + \sigma^i_{xx(yy)}$ i mS), and the operation frequency is 60 THz. (a) and (b) Purcell factors for $x-$ and $y-$polarized dipoles. (c) Relative strength of the QI in the three-level QE.

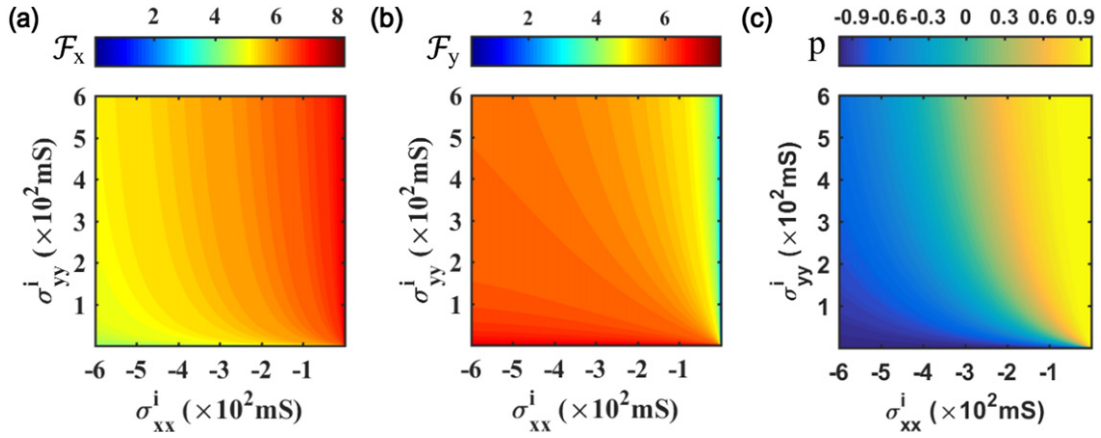

Figure 5. Purcell factors in the logarithmic scale and the relative strength of the QI; both are functions of the surface conductivities ($\sigma_{xx(yy)} = 0.001 + \sigma^i_{xx(yy)}$ i mS). Other parameters are the same as in figure 4. (a) and (b) Purcell factor for $x-$ and $y-$polarized dipoles. (c) Relative strength of the QI in a three-level QE.

Another remarkable feature of the dipole decay is that a prominent anisotropic Purcell effect can also be achieved in the hyperbolic-dispersion case. This is owing to the progressive shift of the hyperbolic branches towards different optical axes as one of the conductivity components becomes considerably larger than the other. Under this condition, the unidirectional excitation of the SPM results in the selective enhancement of the dipole transitions. With a simultaneous increase in the conductivity components, the isofrequency contour moves away from the origin in the $k-$space (green dashed curve in figure 1(d)). Consequently, the metasurface cannot support the coupling of incident waves with small wave numbers, which has a destructive effect on the enhanced Purcell factors. Generally, as indicated by figure 5(c), the launching of highly anisotropic SPMs in the extremely hyperbolic case enables the generation of maximum QI between orthogonal decay channels of the three-level QE.

Finally, we consider the dispersive interaction between three-level QEs and anisotropic black phosphorus metasurfaces to emphasise the experimental implementation of our proposed approach. Heterostructures containing black phosphorus or graphene have been previously identified as good candidates for TDAMs with high tuneabilities [12–14]. In these structures, the intraband excitations owing to carrier motions can be well described by the Drude model [74], where the interband transitions at higher frequencies are included by introducing the step-absorption function. Based on the above features, the anisotropic conductivities of multilayer black phosphorus can be approximately defined as follows [75]:

$$\sigma_{jj} = \frac{\mathrm{i}n_c e^2}{m_j(\omega + \mathrm{i}\tau)} + \mathcal{I}_j\left[\Theta(\omega - \varpi_j) + \frac{\mathrm{i}}{\pi}\ln\frac{|\omega - \varpi_j|}{|\omega + \varpi_j|}\right] \quad (j = x, y), \tag{14}$$

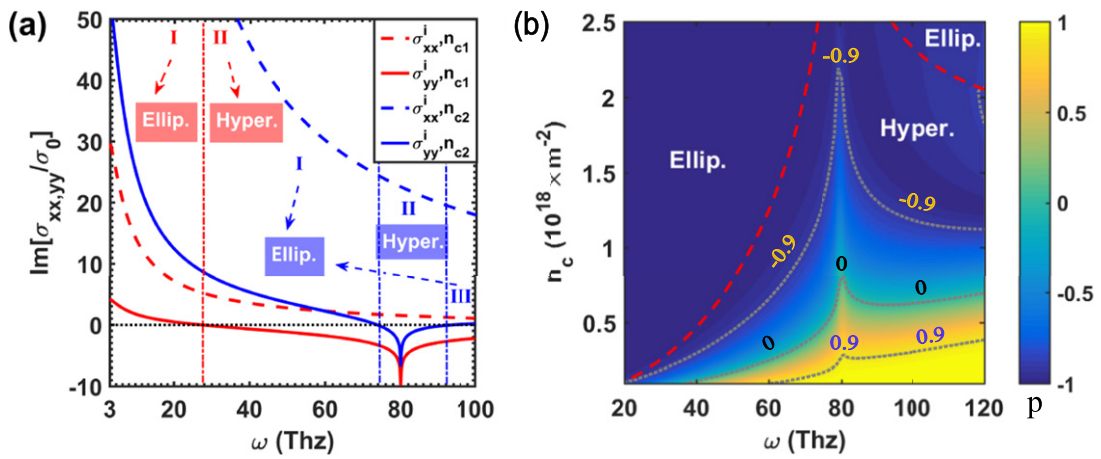

Figure 6. (a) Imaginary part of the conductivity components σ^i_{xx} and σ^i_{yy} as a function of the excitation frequency. The cases of $n_{c1} = 2 \times 10^{17}$ m^{-2} and $n_{c2} = 2.5 \times 10^{18}$ m^{-2} are studied, where different dispersion regimes are marked. The parameters of the TDAM are: $m_x = 0.2m_0$, $m_y = 0.9m_0$, $\tau = 2.5$ THz, $\varpi_x = 240$ THz, $\varpi_y = 80$ THz, $\mathcal{I}_x = 1.5\sigma_0$, and $\mathcal{I}_y = 3.5\sigma_0$. m_0 is the free electron mass, and $\sigma_0 = e^2/4\hbar$ is the conductance quantum. (b) Relative strength of the QI (p) in the three-level QE manipulated by the carrier concentration (n_c) under different transition frequencies.

where the first and second terms on the right-hand side describe the contributions from the intraband and interband transitions, respectively. The effective mass of the electron along the j direction is denoted by m_j, τ is the intraband relaxation rate, and ϖ_j and $\mathcal{I}_j$ represent the resonant frequencies and relevant strengths of the interband transitions for the jj component of the conductivity tensor, respectively. The carrier concentration of the TDAM, which is denoted by n_c in our notation, is experimentally tuneable via bias voltage or chemical doping [76, 77].

Before studying the QI property of the proposed system, it is necessary to clarify the dependence of the surface topology on the carrier concentration n_c. It is clearly demonstrated in figure 6(a) that both the elliptic and hyperbolic topologies (with abbreviations Ellip. and Hyper.) can be achieved under different conditions. At low carrier concentrations, the optical response of the TDAM is weak (red curves), and fewer electrons participate in the collective oscillation of plasmons. In this case, a relatively low phase-transition frequency between two dispersion topologies can be observed (red dash-dotted line). With an increase in frequency, the interband transition becomes dominant, thereby leading to a sharp negative dip in the imaginary part of the conductivity σ^i_{yy}. At large carrier concentrations (blue curves), the optical response of the TDAM becomes considerably stronger. Therefore, a blue-shift of the hyperbolic dispersion regime can be clearly identified.

In figure 6(b), we present a contour plot to illustrate the issue of how a TDAM modifies the relative strength of the QI. Clearly, the strength of the QI can be effectively controlled by manipulating the carrier concentration of the metasurface. It is shown that the critical frequency accounting for the phase change of the surface topology suffers shifts according to the variation of the carrier concentration (red dashed curve). At lower frequencies (20–40 THz), the QI strength gradually increases with an increase in the carrier concentration. This behaviour can be well explained by including the results shown in figure 6(a), where the metasurface supports strong excitations of a highly anisotropic plasmon field in the extremely elliptic regime.

Moreover, when the metasurface works in the hyperbolic regime, the dependence of the QI strength on the carrier concentration exhibits rich features. In general, the QI strength reaches both the positive and negative maximums by crossing zero as the excitation frequency varies. This is owing to the dominant contributions of the interband transition at high frequencies, which even forms a dip in the conductivity near the interband transition frequency ϖ_y (as shown in figure 6(a)). It may seem somewhat counterintuitive that, according to equation (14), an infinite dip occurs at the frequency ϖ_y. However, this does not occur. For real materials, the interband scattering also contributes to conductivity, which only allows the appearance of the dip with a finite depth [78]. However, the scattering rate only broadens the transition width and does not affect the main physics. Thus, for simplicity, we have omitted it in the approximated form of the conductivity. According to figure 6(a), the optical property of the metasurface experiences dramatic changes as a response to the variation in carrier concentration, ranging from the case of $|\sigma^i_{yy}| \gg |\sigma^i_{xx}|$ to $|\sigma^i_{xx}| \gg |\sigma^i_{yy}|$ in the hyperbolic regime. As discussed previously, in both cases, the metasurface supports strong enhancements of the anisotropic Purcell effects with respect to $\mathcal{F}_x \gg \mathcal{F}_y$ and $\mathcal{F}_y \gg \mathcal{F}_x$, which adequately explains the behaviour of the QI by manipulating the carrier concentration.

4. Conclusions and outlook

This study investigates the excitation of the anisotropic SPM and its influence on the Purcell effect as well as the QI effect between the orthogonal decay channels of a three-level QE in the presence of a TDAM. The Green functions of the electric field for the system under consideration are derived to numerically study the excitation features of the SPM and its influence on the QI effect. The numerical results predict the anisotropic excitation of the in-plane field amplitudes, which is in good agreement with the simulation results. We have extended this remarkable feature to the generation and enhancement of QI. To provide a deeper insight, the anisotropic Purcell effect modified by metasurfaces is also investigated. We have shown that the in-plane transitions can be unequally enhanced, owing to the anisotropic excitation of the SPM. Furthermore, in extremely anisotropic cases, the metasurfaces even support a strong enhancement of the anisotropic Purcell effect, which is the main reason for the appearance of maximum QI.

An important aspect of our study consists in showing that the relative strength of QI in three-level QEs coupled with a TDAM can be effectively controlled by engineering the anisotropy of metasurfaces. In real TDAMs, the in-plane anisotropy is determined by the conductivity tensor. As we have presented in section 3, the experimental implementation of the proposed system also demonstrates the feasibility of realizing maximum QI with a flexible manipulation in the carrier concentration of the materials. Our study can be extended to other coupled systems with similar configurations [79, 80]; thus, it provides a promising route in the development of highly integrated photonic devices at the nanoscale [81], which may have potential applications in various quantum technologies.

Acknowledgments

We acknowledge support from the National Natural Science Foundation of China (NSFC, Grant Numbers 11874287, 11947044 and 12104169); the National Key Research and Development Program of China (2021YFA1400602); the Fujian Provincial Natural Science Foundation of China (2022J01292); and the Scientific Research Funds of Huaqiao University (Project Numbers 605-50Y19046 and 605-50Y21003).

Data availability statement

The data that support the findings of this study are available upon reasonable request from the authors.

Appendix A. Derivation of the Green functions

Consider multi-layered structures constructed by piecewise-constant materials. In the presence of an electric current, the electric and magnetic fields in region n can be generally expressed as [67]

$$\mathbf{E}_n(\mathbf{r}) = \left(k_n^2 + \boldsymbol{\nabla}\boldsymbol{\nabla}\cdot\right)\boldsymbol{\Pi}_n(\mathbf{r}), \tag{A.1}$$

$$\mathbf{H}_n(\mathbf{r}) = \mathrm{i}\omega\varepsilon_n\boldsymbol{\nabla}\times\boldsymbol{\Pi}_n(\mathbf{r}), \tag{A.2}$$

where $\varepsilon_n(\mu_n)$ is the relative permittivity (permeability), and $k_n = \omega\sqrt{\varepsilon_n\mu_n}$ and $\boldsymbol{\Pi}_n(\mathbf{r})$ are the wave number and electric Hertzian potential in the region n, respectively. In this study we consider $\varepsilon_2 = \varepsilon_1$ and $\mu_2 = \mu_1$ with the assumption that the permittivity and permeability of the host medium are equal to the vacuum values. We assume that the current source exists in the region 1 with time dependence $\mathrm{e}^{\mathrm{i}\omega t}$, and it is denoted by $\mathbf{j}_1$. Then, in the single-layered case, the Hertzian potentials in the upper (region 1) and lower (region 2) spaces are

$$\begin{aligned}\boldsymbol{\Pi}_1(\mathbf{r}) &= \boldsymbol{\Pi}_1^P(\mathbf{r}) + \boldsymbol{\Pi}_1^S(\mathbf{r})\\ &= \int_\Omega \left\{\bar{\mathbf{g}}_1^P(\mathbf{r},\mathbf{r}') + \bar{\mathbf{g}}_1^R(\mathbf{r},\mathbf{r}')\right\}\cdot\frac{\mathbf{j}_1(\mathbf{r}')}{i\omega\varepsilon_1}\,\mathrm{d}\Omega',\end{aligned} \tag{A.3}$$

$$\boldsymbol{\Pi}_2(\mathbf{r}) = \boldsymbol{\Pi}_2^S(\mathbf{r}) = \int_\Omega \bar{\mathbf{g}}_2^T(\mathbf{r},\mathbf{r}')\cdot\frac{\mathbf{j}_1(\mathbf{r}')}{i\omega\varepsilon_1}\,\mathrm{d}\Omega'. \tag{A.4}$$

In the above equations, $\boldsymbol{\Pi}_1^P(\mathbf{r})$ is the principle part (free propagating modes induced by the electric current without boundary reflections) of the Hertzian potential due to the existence of the current source in the

upper space (region 1), and $\mathbf{\Pi}_n^S(\mathbf{r})$ denotes the scattered potentials in different spatial regions. The principle part of the corresponding Green's dyadic is denoted by $\bar{\mathbf{g}}_1^P(\mathbf{r},\mathbf{r}')$, where $\bar{\mathbf{g}}_1^R(\mathbf{r},\mathbf{r}')$ represents the reflection part that is responsible for the fields reflected by the layered-material, $\bar{\mathbf{g}}_1^T(\mathbf{r},\mathbf{r}')$ is the transmission part owing to the field penetrations through the metasurface scattered into the lower space (region 2), and Ω is the support of the current. In our notation, the principle part of Green's dyadic can be written as

$$\begin{aligned}\bar{\mathbf{g}}_1^P(\mathbf{r},\mathbf{r}') &= \bar{\mathbf{I}}\frac{\mathrm{e}^{-\mathrm{i}k_1R}}{4\pi R}\\ &= \bar{\mathbf{I}}\frac{\mathrm{i}}{(2\pi)^2}\int_{-\infty}^{\infty}\frac{\mathrm{e}^{\mathrm{i}\beta_1|z-z'|}}{2\beta_1}\,\mathrm{e}^{-\mathrm{i}\mathbf{k}\cdot(\rho-\rho')}\,\mathrm{d}\mathbf{k},\end{aligned} \tag{A.5}$$

where $\mathbf{k}=k_x\mathbf{e}_x+k_y\mathbf{e}_y$ is the in-plane wave vector with a magnitude denoted by $|\mathbf{k}|=k=\sqrt{k_x^2+k_y^2}$, and its $z-$component is $\beta_1=\sqrt{k_1^2-k^2}$. $\boldsymbol{\rho}=x\mathbf{e}_x+y\mathbf{e}_y$ is the in-plane component of the position vector $\mathbf{r}=(x,y,z)$, which can be varied when evaluating the electric field at different spatial points (similarly, $\mathbf{r}'=(x',y',z')$ and $\boldsymbol{\rho}'$ denote the position vectors of the current source). $\bar{\mathbf{I}}$ is the unit dyadic, the distance between the field and source points ($\mathbf{r}$ and $\mathbf{r}'$) is denoted by $R=\sqrt{\rho^2+(z-z')^2}$, with $\rho=\sqrt{(x-x')^2+\left(y-y'\right)^2}$ representing its projection on the x–y plane. The scattered part of Green's dyadic can be obtained by applying the following boundary conditions:

$$\hat{\mathbf{z}}\times[\mathbf{H}_1-\mathbf{H}_2]=\mathbf{J}_s, \tag{A.6}$$

$$\hat{\mathbf{z}}\times[\mathbf{E}_1-\mathbf{E}_2]=0, \tag{A.7}$$

where $\mathbf{J}_s=\bar{\sigma}\cdot\mathbf{E}$ is the electric surface current on the boundary. We introduce the two-dimensional Fourier transform on the vector potential:

$$\mathbf{\Pi}_n(\mathbf{k},z)=\int_{-\infty}^{\infty}\int_{-\infty}^{\infty}\mathbf{\Pi}_n(\mathbf{r})\mathrm{e}^{\mathrm{i}\mathbf{k}\cdot\mathbf{r}}\,\mathrm{d}x\,\mathrm{d}y, \tag{A.8}$$

$$\mathbf{\Pi}_n(\mathbf{r})=\frac{1}{(2\pi)^2}\int_{-\infty}^{\infty}\int_{-\infty}^{\infty}\mathbf{\Pi}_n(\mathbf{k},z)\mathrm{e}^{-\mathrm{i}\mathbf{k}\cdot\mathbf{r}}\,\mathrm{d}k_x\,\mathrm{d}k_y, \tag{A.9}$$

and substitute the Hertzian potential $\mathbf{\Pi}_n(\mathbf{r})$ into the boundary conditions given in equations (A.6) and (A.7). After rearranging, we obtain the following equations:

$$k_1^2\mathbf{\Pi}_{1j}(\mathbf{r})-\mathrm{i}k_j\boldsymbol{\nabla}\cdot\mathbf{\Pi}_1(\mathbf{r})=k_2^2\mathbf{\Pi}_{2j}(\mathbf{r})-\mathrm{i}k_j\boldsymbol{\nabla}\cdot\mathbf{\Pi}_2(\mathbf{r}), \tag{A.10}$$

$$\sum_{n=1,2}(-1)^n\mathrm{i}\omega\varepsilon_n\left(\frac{\partial\mathbf{\Pi}_{nj}(\mathbf{r})}{\partial z}+\mathrm{i}k_j\mathbf{\Pi}_{nz}(\mathbf{r})\right)=\sigma_{jj}[k_1^2\mathbf{\Pi}_{1j}(\mathbf{r})-\mathrm{i}k_j\nabla\cdot\mathbf{\Pi}_1(\mathbf{r})].(j=x,y). \tag{A.11}$$

In the above equations, $\mathbf{\Pi}_{nj}(\mathbf{r})$ represents the j component of the Hertzian potential in the region n, and the relation $k_1=k_2$ is satisfied for the model under consideration. Different from the isotropic case, wherein the $z-$directed current only induces the potential $\mathbf{\Pi}_{nz}(\mathbf{r})$, in the presence of anisotropic surfaces, the vertical current also induces the potentials $\mathbf{\Pi}_{nx}(\mathbf{r})$ and $\mathbf{\Pi}_{ny}(\mathbf{r})$. Combined with the property that the in-plane currents induce both the horizontal and vertical potentials (i.e., $\mathbf{\Pi}_{nx}(\mathbf{r})$ and $\mathbf{\Pi}_{nz}(\mathbf{r})$ for the $x-$directed current, $\mathbf{\Pi}_{ny}(\mathbf{r})$ and $\mathbf{\Pi}_{nz}(\mathbf{r})$ for the $y-$directed current), according to (A.10) and (A.11), the equations for the potentials $\mathbf{\Pi}_{nx}(\mathbf{r})$ and $\mathbf{\Pi}_{nz}(\mathbf{r})$ can be easily determined:

$$\mathbf{\Pi}_{1x}(\mathbf{r})=\mathbf{\Pi}_{2x}(\mathbf{r}), \tag{A.12}$$

$$\frac{\partial\mathbf{\Pi}_{1z}(\mathbf{r})}{\partial z}=\frac{\partial\mathbf{\Pi}_{2z}(\mathbf{r})}{\partial z}, \tag{A.13}$$

$$k_x\omega\varepsilon_1[\mathbf{\Pi}_{2z}(\mathbf{r})-\mathbf{\Pi}_{1z}(\mathbf{r})]-\mathrm{i}\sigma_{xx}k_x\frac{\partial\mathbf{\Pi}_{1z}(\mathbf{r})}{\partial z}=\mathrm{i}\omega\varepsilon_1\left[\frac{\partial\mathbf{\Pi}_{2x}(\mathbf{r})}{\partial z}-\frac{\partial\mathbf{\Pi}_{1x}(\mathbf{r})}{\partial z}\right]-\sigma_{xx}\left(k_1^2-k_x^2\right)\mathbf{\Pi}_{1x}(\mathbf{r}), \tag{A.14}$$

$$k_y\omega\varepsilon_1[\mathbf{\Pi}_{2z}(\mathbf{r})-\mathbf{\Pi}_{1z}(\mathbf{r})]-\mathrm{i}\sigma_{yy}k_y\frac{\partial\mathbf{\Pi}_{1z}(\mathbf{r})}{\partial z}=\sigma_{yy}k_xk_y\mathbf{\Pi}_{1x}(\mathbf{r}). \tag{A.15}$$

It should be noted that equations (A.12)–(A.15) are legal when considering the electric field excited by the $x-$ and $z-$directed current sources. For example, by assuming an $x-$directed current source in the upper space, we obtain the following relations for the scattered coefficients of Green's dyadic:

$$1+g_{xx}^{R}(\mathbf{k})=g_{xx}^{T}(\mathbf{k}), \tag{A.16}$$

$$g_{zx}^{R}(\mathbf{k})=-g_{zx}^{T}(\mathbf{k}), \tag{A.17}$$

$$k_x\omega\varepsilon_1\left[g_{zx}^{T}(\mathbf{k})-g_{zx}^{R}(\mathbf{k})\right]+k_x\beta_1\sigma_{xx}g_{zx}^{R}(\mathbf{k})=\beta_1\omega\varepsilon_1\left[g_{xx}^{R}(\mathbf{k})+g_{xx}^{T}(\mathbf{k})-1\right]-\sigma_{xx}\left(k_1^2-k_x^2\right)\left[1+g_{xx}^{R}(\mathbf{k})\right], \tag{A.18}$$

$$k_y\omega\varepsilon_1\left[g_{zx}^{T}(\mathbf{k})-g_{zx}^{R}(\mathbf{k})\right]+k_y\beta_1\sigma_{yy}g_{zx}^{R}(\mathbf{k})=\sigma_{yy}k_xk_y\left[1+g_{xx}^{R}(\mathbf{k})\right]. \tag{A.19}$$

Here, the superscripts R and T in the coefficients denote the reflection and transmission parts of the field, respectively. Following the methods mentioned above, the equations for the other scattered coefficients can also be derived. Finally, the integrals related to the scattered Green's dyadic takes the following form:

$$\bar{\mathbf{g}}^{S}(\mathbf{r},\mathbf{r}')=\frac{\mathrm{i}}{(2\pi)^2}\int_{-\infty}^{\infty}\int_{-\infty}^{\infty}\begin{pmatrix}g_{xx}^{S}(\mathbf{k}) & 0 & g_{xz}^{S}(\mathbf{k})\\ 0 & g_{yy}^{S}(\mathbf{k}) & g_{yz}^{S}(\mathbf{k})\\ g_{zx}^{S}(\mathbf{k}) & g_{zy}^{S}(\mathbf{k}) & g_{zz}^{S}(\mathbf{k})\end{pmatrix}\frac{\mathrm{e}^{\mathrm{i}\beta_1(z+z')}}{2\beta_1}\mathrm{e}^{-\mathrm{i}\mathbf{k}\cdot(\rho-\rho')}\,\mathrm{d}k_x\,\mathrm{d}k_y.\quad(S=R,T). \tag{A.20}$$

The scattered coefficient $g_{ji}^{R}(\mathbf{k})$ in equation (A.20) clearly contributes to the electric field in the upper space. In the following, we provide detail expressions of the terms $g_{xx}^{R}(\mathbf{k})$, $g_{yy}^{R}(\mathbf{k})$, $g_{zx}^{R}(\mathbf{k})$, and $g_{zy}^{R}(\mathbf{k})$, which are important for obtaining the results of this study:

$$g_{xx}^{R}(\mathbf{k})=\left[2k_1^2\sigma_{xx}-2k_x^2\left(\sigma_{xx}-\sigma_{yy}\right)-k_1\beta_1\sigma_{xx}\sigma_{yy}\eta\right]/\mathrm{D}(\mathbf{k}), \tag{A.21}$$

$$g_{yy}^{R}(\mathbf{k})=\left[2k_y^2\sigma_{xx}-2\left(k_y^2-k_1^2\right)\sigma_{yy}-k_1\beta_1\sigma_{xx}\sigma_{yy}\eta\right]/\mathrm{D}(\mathbf{k}), \tag{A.22}$$

$$g_{zx}^{R}(\mathbf{k})=-2\beta_1k_x\sigma_{yy}/\mathrm{D}(\mathbf{k}), \tag{A.23}$$

$$g_{zy}^{R}(\mathbf{k})=-2\beta_1k_y\sigma_{xx}/\mathrm{D}(\mathbf{k}). \tag{A.24}$$

In equations (A.21)–(A.24) the coefficient $\eta=\sqrt{\mu_1/\varepsilon_1}$, the denominator of the Green functions, defined as $\mathrm{D}(\mathbf{k})=2\sigma_{xx}\left(k_x^2-k_1^2\right)+2\sigma_{yy}\left(k_y^2-k_1^2\right)+4\beta_1k_1\eta^{-1}\left(1+\sigma_{xx}\sigma_{yy}\eta^2/4\right)$, determines the dispersion of the SPM supported by the TDAM, where the dispersion relation in equation (2) can be acquired by solving $\mathrm{D}(\mathbf{k})=0$. After combining equations (A.1) and (A.20)–(A.24), the Green functions in the spatial domain are as follows:

$$\begin{aligned}\bar{\mathbf{G}}_{xx}(\mathbf{r},\mathbf{r}')\big|_{\mathbf{r},\mathbf{r}'>0}&=\bar{\mathbf{G}}_{xx}^{P}(\mathbf{r},\mathbf{r}')+\bar{\mathbf{G}}_{xx}^{R}(\mathbf{r},\mathbf{r}')\\&=\bar{\mathbf{G}}_{xx}^{P}(\mathbf{r},\mathbf{r}')+\frac{1}{2\pi}\int_{-\infty}^{\infty}\mathrm{e}^{-\mathrm{i}k_y(y-y')}f_{xx}(k_y)\mathrm{d}k_y,\end{aligned} \tag{A.25}$$

$$\begin{aligned}\bar{\mathbf{G}}_{yy}(\mathbf{r},\mathbf{r}')\big|_{\mathbf{r},\mathbf{r}'>0}&=\bar{\mathbf{G}}_{yy}^{P}(\mathbf{r},\mathbf{r}')+\bar{\mathbf{G}}_{yy}^{R}(\mathbf{r},\mathbf{r}')\\&=\bar{\mathbf{G}}_{yy}^{P}(\mathbf{r},\mathbf{r}')+\frac{1}{2\pi}\int_{-\infty}^{\infty}\mathrm{e}^{-\mathrm{i}k_y(y-y')}f_{yy}(k_y)\mathrm{d}k_y,\end{aligned} \tag{A.26}$$

$$\bar{\mathbf{G}}_{zz(xx,yy)}^{P}(\mathbf{r},\mathbf{r}')=\frac{\mathrm{i}}{2\pi}\int_{-\infty}^{\infty}\frac{k^3\,\mathrm{e}^{\mathrm{i}\beta_1|z-z'|}J_0(k\rho)}{2\beta_1}\mathrm{d}k. \tag{A.27}$$

In the above expressions, $J_0(k\rho)$ is the zero-order Bessel function, $\bar{\mathbf{G}}_{jj}^{P}(\mathbf{r},\mathbf{r}')$ and $\bar{\mathbf{G}}_{jj}^{R}(\mathbf{r},\mathbf{r}')(j=x,y)$ represent the principle and reflection parts, respectively, where the latter is modified by the metasurfaces and becomes predominant for strong plasmon field excitations. The inner integral functions are

$$f_{xx}(k_y)=\frac{\mathrm{i}}{2\pi}\int_{-\infty}^{\infty}g_{xx}^{R}(k_x,k_y)\frac{\left(k_1^2-k_x^2\right)\mathrm{e}^{\mathrm{i}\beta_1(z+z')}}{2\beta_1}\mathrm{e}^{-\mathrm{i}k_x(x-x')}\,\mathrm{d}k_x, \tag{A.28}$$

$$f_{yy}(k_y)=\frac{\mathrm{i}}{2\pi}\int_{-\infty}^{\infty}g_{yy}^{R}(k_x,k_y)\frac{\left(k_1^2-k_y^2\right)\mathrm{e}^{\mathrm{i}\beta_1(z+z')}}{2\beta_1}\mathrm{e}^{-\mathrm{i}k_x(x-x')}\,\mathrm{d}k_x. \tag{A.29}$$

Based on the definitions in equations (11) and (12), it is clear that the Green functions in equations (A.25)–(A.27) play a key role in evaluating the spontaneous decay rates of dipoles with different polarizations. Additionally, we notice that in the presence of a TDAM (the boundary conditions are given in equations (A.10) and (A.11)), for a unit strength current source, the $x-$ and $y-$component of the excited field can be expressed as follows:

$$\mathbf{E}_j=\frac{1}{\mathrm{i}\omega\varepsilon_0}\left[\bar{\mathbf{G}}_{jj}(\mathbf{r},\mathbf{r}')+\bar{\mathbf{G}}_{zj}(\mathbf{r},\mathbf{r}')\right]\big|_{\mathbf{r},\mathbf{r}'>0}\quad(j=x,y), \tag{A.30}$$

where the off-diagonal Green functions take the following forms:

$$\bar{\mathbf{G}}_{zx}(\mathbf{r},\mathbf{r}')\big|_{\mathbf{r},\mathbf{r}'>0} = \frac{\partial^2}{\partial z\partial x}\bar{\mathbf{g}}^R_{zx}(\mathbf{r},\mathbf{r}') = \frac{\mathrm{i}}{8\pi^2}\int_{-\infty}^{\infty}\int_{-\infty}^{\infty} g^R_{zx}(\mathbf{k})k_x\,\mathrm{e}^{\mathrm{i}\beta_1(z+z')}\,\mathrm{e}^{-\mathrm{i}\mathbf{k}\cdot(\boldsymbol{\rho}-\boldsymbol{\rho}')}\,\mathrm{d}k_x\,\mathrm{d}k_y, \tag{A.31}$$

$$\bar{\mathbf{G}}_{zy}(\mathbf{r},\mathbf{r}')\big|_{\mathbf{r},\mathbf{r}'>0} = \frac{\partial^2}{\partial z\partial y}\bar{\mathbf{g}}^R_{zy}(\mathbf{r},\mathbf{r}') = \frac{\mathrm{i}}{8\pi^2}\int_{-\infty}^{\infty}\int_{-\infty}^{\infty} g^R_{zy}(\mathbf{k})k_y\,\mathrm{e}^{\mathrm{i}\beta_1(z+z')}\,\mathrm{e}^{-\mathrm{i}\mathbf{k}\cdot(\boldsymbol{\rho}-\boldsymbol{\rho}')}\,\mathrm{d}k_x\,\mathrm{d}k_y. \tag{A.32}$$

Appendix B. Approximation method adopted in the numerical calculations

As indicated in equations (A.25)–(A.32), a numerical evaluation of the Green functions is time-consuming, owing to the two-dimensional feature of the integrals. However, we are primarily interested in the strong QE-SPM coupling cases; therefore, it is feasible to describe the contribution of the SPM by only keeping the residue part of the integrals. Within this approximation, the integrals can be reduced to one-dimensional; thus, a considerable acceleration in the speed of numerical evaluation can be expected. To verify the validity of this method, we present an example that considers the integral defined in equation (A.28), where the dispersion of the SPM is solely determined by the zeros of the denominator in the reflection coefficient $g^R_{xx}(\mathbf{k})$.

For specific values of k_y, we assume that the roots of $\mathrm{D}(\mathbf{k}) = 0$ can be denoted by k_x^{sp}. k_x^{sp} are functions of k_y, according to the definition of $\mathrm{D}(\mathbf{k})$. Notably, there are four solutions (accounting for the modes with different wave numbers and propagating features) of the supported wave modes k_x^{sp} for every k_y; however, only one of them is allowed under particular conditions. For example, the relation $\mathrm{Im}\left[k_x^{sp}\right] < 0$ must be satisfied to obtain a decaying wave that propagates away from the source for the spatial region $(x - x') > 0$. In this case, the residue contribution of the SPM on the integral $f_{xx}(k_y)$ (defined in equation (A.28)) takes the following form:

$$f^{\mathrm{Res}}_{xx}(k_y) = \frac{g^R_{xx}(k_x^{sp},k_y)}{2\beta_1^{sp}}\left[k_1^2 - (k_x^{sp})^2\right]\mathrm{e}^{\mathrm{i}\beta_1^{sp}(z+z')}\,\mathrm{e}^{-\mathrm{i}k_x^{sp}(x-x')}, \tag{B.1}$$

where $\beta_1^{sp} = \sqrt{k_1^2 - (k_x^{sp})^2 - k_y^2}$ and the residue form of the reflection coefficient can be defined through

$$g^R_{xx}(k_x^{sp},k_y) = \left[2k_1^2\sigma_{xx} - 2k_x^2(\sigma_{xx}-\sigma_{yy}) - k_1\beta_1^{sp}\sigma_{xx}\sigma_{yy}\eta\right]\frac{\partial \mathrm{D}(\mathbf{k})}{\partial k_x}^{-1}\Big|_{k_x=k_x^{sp}}. \tag{B.2}$$

In figure B1 we compare the exact numerical result and the residue contribution of the function $f_{xx}(k_y)$, where the former is obtained by performing the integral defined in equation (A.28), and the latter is obtained by simply evaluating the residue term in equation (B.1) as functions of the in-plane wave number k_y. The QE is located at a distance of $z_a = 10^{-3}\lambda_a$ above the anisotropic metasurface, and different behaviours of the integrand are studied. Subplot (a) demonstrates the imaginary part of the integral function $f_{xx}(k_y)$ versus k_y at $x = 0$. In this case, only the imaginary part of the Green functions evaluated at the spatial position $\mathbf{r}_a = (0, 0, 10^{-3}\lambda_a)$ contributes to the spontaneous decay of the QE (see equation (A.25)). We note that, except for a subtle difference in the magnitude at small k_y and a slight shift in the phase space, the residue approximation is in good agreement with the exact numerical result.

Additional to the source point, the validity of the approximated method under the influence of the propagating SPM is also studied by evaluating the integral function at $x = 0.1\lambda_a$. Under this condition, the integrand oscillates, owing to the nonvanished factor $\mathrm{e}^{-\mathrm{i}k_x^{sp}(x-x')}$. Similarly, as demonstrated in subfigure (c) of figure B1, it is clear that the approximation method possesses high accuracy in evaluating the integral. Within this approximation, we obtain figures 4–6 by numerically evaluating the Green functions. Notably, the approximation method is valid only when the coupling between the QE and SPM makes a dominant contribution to the spontaneous decay [70]. If the QE is too close to the surface, the spontaneous decay process will primarily occur via material dissipation [82]. In another case, where the QE is far from the metasurface, the branch-cut term [83] of equation (A.28) that describes the radiation continuum into space cannot be neglected when performing the integral.

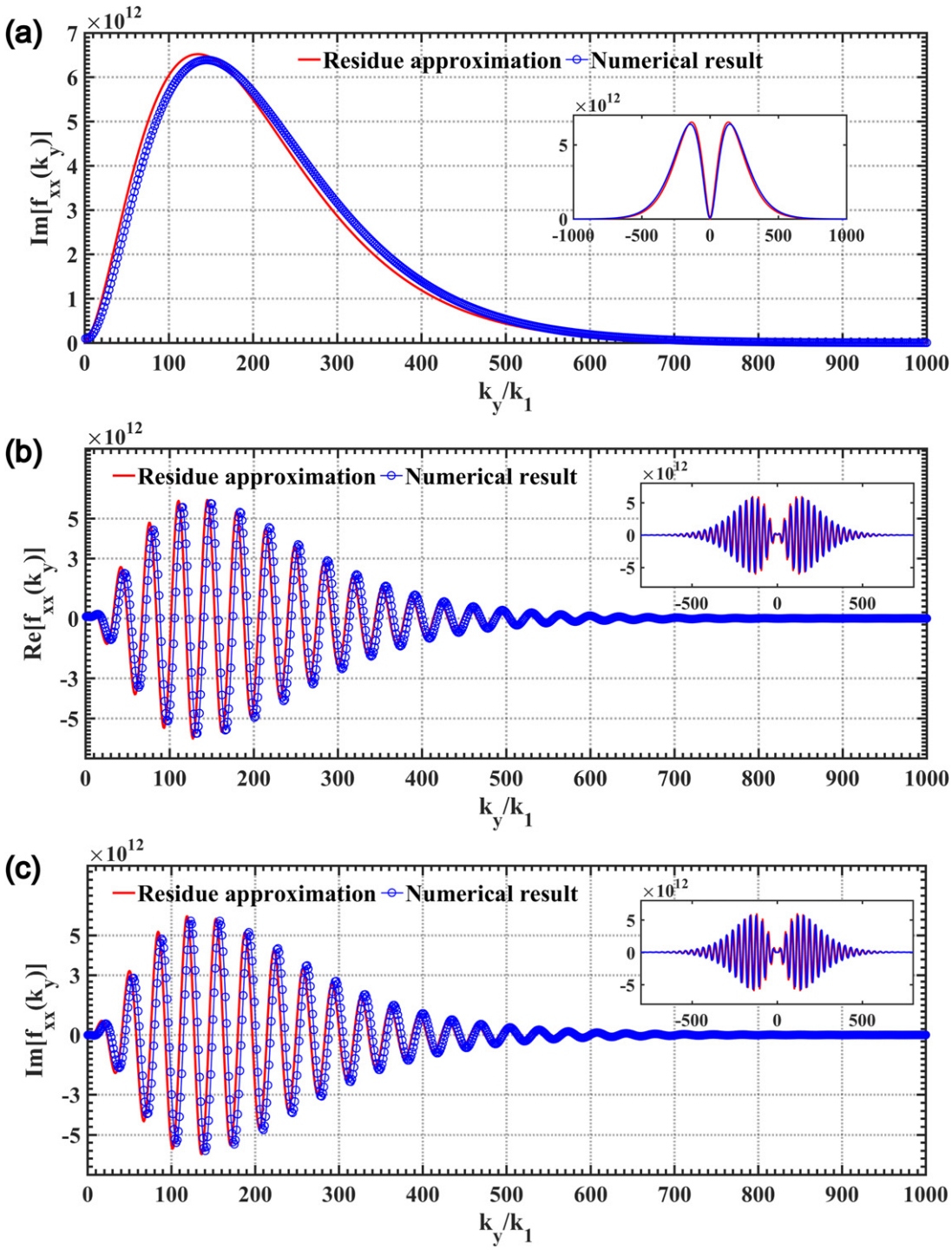

Figure B1. The integral function $f_{xx}(k_y)$ evaluated using different methods under the condition: $\sigma_{xx} = 0.001 + 6\mathrm{i}$ mS, $\sigma_{yy} = 0.001 - 2\mathrm{i}$ mS, $\mathbf{r}_a = (0, 0, 10^{-3}\lambda_a)$, where the operation frequency is 60 THz. (a) Imaginary part of the integral function with $x = 0$. (b) and (c) Real and imaginary parts of the integral function with $x = 0.1\lambda_a$.

ORCID iDs

Gao-xiang Li https://orcid.org/0000-0002-2906-7503

References

[1] Goossens S *et al* 2017 Broadband image sensor array based on graphene-CMOS integration *Nat. Photon.* **11** 366–71
[2] Smit M, Williams K and van der Tol J 2019 Past, present, and future of InP-based photonic integration *APL Photon.* **4** 050901
[3] Wu Y *et al* 2019 Monolithic integration of MoS_2-based visible detectors and GaN-based UV detectors *Photon. Res.* **7** 1127–33
[4] Low T *et al* 2017 Polaritons in layered two-dimensional materials *Nat. Mater.* **16** 182–94

[5] Woessner A et al 2015 Highly confined low-loss plasmons in graphene-boron nitride heterostructures Nat. Mater. 14 421–5
[6] Lin X, Rivera N, López J J, Kaminer I, Chen H and Soljačić M 2016 Tailoring the energy distribution and loss of 2D plasmons New J. Phys. 18 105007
[7] Kumada N, Dubourget R, Sasaki K, Tanabe S, Hibino H, Kamata H, Hashisaka M, Muraki K and Fujisawa T 2014 Plasmon transport and its guiding in graphene New J. Phys. 16 063055
[8] Wehling T O, Novoselov K S, Morozov S V, Vdovin E E, Katsnelson M I, Geim A K and Lichtenstein A I 2008 Molecular doping of graphene Nano Lett. 8 173–7
[9] Ye L, Sui K, Liu Y, Zhang M and Liu Q H 2018 Graphene-based hybrid plasmonic waveguide for highly efficient broadband mid-infrared propagation and modulation Opt. Express 26 15935–47
[10] Ju L et al 2011 Graphene plasmonics for tunable terahertz metamaterials Nat. Nanotechnol. 6 630–4
[11] Koppens F H L, Mueller T, Avouris P, Ferrari A C, Vitiello M S and Polini M 2014 Photodetectors based on graphene, other two-dimensional materials and hybrid systems Nat. Nanotechnol. 9 780–93
[12] Trushkov I and Iorsh I 2015 Two-dimensional hyperbolic medium for electrons and photons based on the array of tunnel-coupled graphene nanoribbons Phys. Rev. B 92 045305
[13] Low T, Rodin A S, Carvalho A, Jiang Y J, Wang H, Xia F N and Neto A H C 2014 Tunable optical properties of multilayers black phosphorus thin films Phys. Rev. B 90 075434
[14] Xia F, Wang H and Jia Y 2014 Rediscovering black phosphorus as an anisotropic layered material for optoelectronics and electronics Nat. Commun. 5 4458
[15] Li P et al 2018 Infrared hyperbolic metasurface based on nanostructured van der Waals materials Science 359 892–6
[16] High A A, Devlin R C, Dibos A, Polking M, Wild D S, Perczel J, de Leon N P, Lukin M D and Park H 2015 Visible-frequency hyperbolic metasurface Nature 522 192–6
[17] Yermakov O Y, Hurshkainen A A, Dobrykh D A, Kapitanova P V, Iorsh I V, Glybovski S B and Bogdanov A A 2018 Experimental observation of hybrid TE-TM polarized surface waves supported by a hyperbolic metasurface Phys. Rev. B 98 195404
[18] Paul N K and Gomez-Diaz J S 2021 Broadband and unidirectional plasmonic hyperlensing in drift-biased graphene Appl. Phys. Lett. 118 091107
[19] Chen P-Y, Soric J, Padooru Y R, Bernety H M, Yakovlev A B and Alù A 2013 Nanostructured graphene metasurface for tunable terahertz cloaking New J. Phys. 15 123029
[20] Xiong L et al 2019 Photonic crystal for graphene plasmons Nat. Commun. 10 4780
[21] Zhang Y, Antezza M, Yi H L and Tan H P 2019 Metasurface-mediated anisotropic radiative heat transfer between nanoparticles Phys. Rev. B 100 085426
[22] Ménard-Moyon C, Bianco A and Kalantar-Zadeh K 2020 Two-dimensional material-based biosensors for virus detection ACS Sensors 5 3739–69
[23] Zhao L, Shang Q, Li M, Liang Y, Li C and Zhang Q 2020 Strong exciton–photon interaction and lasing of two-dimensional transition metal dichalcogenide semiconductors Nano Res. 14 1937–54
[24] Cai Y, Xu K-D, Feng N, Guo R, Lin H and Zhu J 2019 Anisotropic infrared plasmonic broadband absorber based on graphene-black phosphorus multilayers Opt. Express 27 3101–12
[25] Shiue R-J, Efetov D K, Grosso G, Peng C, Fong K C and Englund D 2017 Active 2D materials for on-chip nanophotonics and quantum optics Nanophotonics 6 1329–42
[26] Lamb W E and Retherford R C 1947 Fine structure of the hydrogen atom by a microwave method Phys. Rev. 72 241
[27] Purcell E M, Torrey H C and Pound R V 1946 Resonance absorption by nuclear magnetic moments in a solid Phys. Rev. 69 37
[28] Xu J P, Yang Y P, Lin Q and Zhu S Y 2009 Spontaneous decay of a two-level atom near the left-handed slab Phys. Rev. A 79 043812
[29] Lu D, Kan J J, Fullerton E E and Liu Z 2014 Enhancing spontaneous emission rates of molecules using nanopatterned multilayer hyperbolic metamaterials Nat. Nanotechnol. 9 48–53
[30] Cortes C L, Newman W, Molesky S and Jacob Z 2012 Quantum nanophotonics using hyperbolic metamaterials J. Opt. 14 063001
[31] Li L, Zhou Z, Min C and Yuan X 2021 Few-layer metamaterials for spontaneous emission enhancement Opt. Lett. 46 190–3
[32] Lou F, Yan M, Thylen L, Qiu M and Wosinski L 2014 Whispering gallery mode nanodisk resonator based on layered metal-dielectric waveguide Opt. Express 22 8490–502
[33] Perera C S, Vernon K C and Mcleod A 2014 Simulations of the spontaneous emission of a quantum dot near a gap plasmon waveguide J. Appl. Phys. 115 054314
[34] Vasa P and Lienau C 2018 Strong light-matter interaction in quantum emitter/metal hybrid nanostructures ACS Photon. 5 2–23
[35] Kumar S, Leissner T, Boroviks S, Andersen S K H, Fiutowski J, Rubahn H-G, Mortensen N A and Bozhevolnyi S I 2020 Efficient coupling of single organic molecules to channel plasmon polaritons supported by V-grooves in monocrystalline gold ACS Photon. 7 2211–8
[36] Reed M D, Johnson B R, Houck A A, Dicarlo L, Chow J M, Schuster D I, Frunzio L and Schoelkopf R J 2010 Fast reset and suppressing spontaneous emission of a superconducting qubit Appl. Phys. Lett. 96 203110
[37] Javadi A, Maibom S, Sapienza L, Thyrrestrup H, García P D and Lodahl P 2014 Statistical measurements of quantum emitters coupled to Anderson-localized modes in disordered photonic-crystal waveguides Opt. Express 22 30992–1001
[38] Wang Y J, Ren J, Zhang W X, He L and Zhang X D 2020 Topologically protected strong coupling and entanglement between distant quantum emitters Phys. Rev. Appl. 14 054007
[39] Dezfouli M K, Gordon R and Hughes S 2017 Modal theory of modified spontaneous emission of a quantum emitter in a hybrid plasmonic photonic-crystal cavity system Phys. Rev. A 95 013846
[40] Guzatov D V and Klimov V V 2012 The influence of chiral spherical particles on the radiation of optically active molecules New J. Phys. 14 123009
[41] Hakami J, Wang L G and Zubairy M S 2014 Spectral properties of a strongly coupled quantum-dot-metal-nanoparticle system Phys. Rev. A 89 053835
[42] Dzsotjan D, Sorensen A S and Fleischhauer M 2010 Quantum emitters coupled to surface plasmons of a nanowire: a Green's function approach Phys. Rev. B 82 075427
[43] Goban A, Hung C L, Hood J D, Yu S P, Muniz J A, Painter O and Kimble H J 2015 Superradiance for atoms trapped along a photonic crystal waveguide Phys. Rev. Lett. 115 063601
[44] Martin-Cano D, Haakh H R, Murr K and Agio M 2014 Large suppression of quantum fluctuations of light from a single emitter by an optical nanostructure Phys. Rev. Lett. 113 263606
[45] Liu F et al 2018 High Purcell factor generation of indistinguishable on-chip single photons Nat. Nanotechnol. 13 835–40

[46] Chen H Y, Zhang F, Zhao D X, Zhang J X, Xu J P, He Q Y, Gong Q H and Gu Y 2017 Surface-plasmon-enhanced quantum field entanglement through anisotropic Purcell factors *Phys. Rev.* A **96** 043865
[47] Ficek Z and Swain S 2005 *Quantum Interference and Coherence: Theory and Experiments* (Berlin: Springer)
[48] Agarwal G S 2000 Anisotropic vacuum-induced interference in decay channels *Phys. Rev. Lett.* **84** 5500
[49] Mompart J and Corbalán R 2000 Lasing without inversion *J. Opt. B: Quantum Semiclass. Opt.* **2** R7
[50] Derkacz L and Jakobczyk L 2006 Quantum interference and evolution of entanglement in a system of three-level atoms *Phys. Rev.* A **74** 032313
[51] Kumar R, Gokhroo V and Chormaic S N 2015 Multi-level cascaded electromagnetically induced transparency in cold atoms using an optical nanofibre interface *New J. Phys.* **17** 123012
[52] Cheng H, Wang H-M, Zhang S-S, Xin P-P, Luo J and Liu H-P 2017 Electromagnetically induced transparency of ^{87}Rb in a buffer gas cell with magnetic field *J. Phys. B: At. Mol. Opt. Phys.* **50** 095401
[53] Paspalakis E and Knight P L 2001 Localizing an atom via quantum interference *Phys. Rev.* A **63** 065802
[54] Bozorgzadeh F, Fard M R G and Sahrai M 2020 Controllable two- and three-dimensional atom localization via spontaneously generated coherence *Eur. Phys. J. Plus* **135** 904
[55] Zhu S-Y and Scully M O 1996 Spectral line elimination and spontaneous emission cancellation via quantum interference *Phys. Rev. Lett.* **76** 388
[56] Xu J P and Yang Y P 2010 Quantum interference of V-type three-level atom in structures made of left-handed materials and mirrors *Phys. Rev.* A **81** 013816
[57] Yannopapas V, Paspalakis E and Vitanov N V 2009 Plasmon-induced enhancement of quantum interference near metallic nanostructures *Phys. Rev. Lett.* **103** 063602
[58] Zeng X D, Li Z H, Ge G Q and Zubairy M S 2019 Quantum interference near graphene layers: observing the surface plasmons with transverse electric polarization *Phys. Rev.* A **99** 043811
[59] Koenig S P, Doganov R A, Schmidt H, Castro Neto A H and Özyilmaz B 2014 Electric field effect in ultrathin black phosphorus *Appl. Phys. Lett.* **104** 103106
[60] Rodin A S, Carvalho A and Castro Neto A H 2014 Strain-induced gap modification in black phosphorus *Phys. Rev. Lett.* **112** 176801
[61] Petersen R, Pedersen T G and Javier García de Abajo F 2017 Nonlocal plasmonic response of doped and optically pumped graphene, MoS_2, and black phosphorus *Phys. Rev.* B **96** 205430
[62] Schädler K G, Ciancico C, Pazzagli S, Lombardi P, Bachtold A, Toninelli C, Reserbat-Plantey A and Koppens F H L 2019 Electrical control of lifetime-limited quantum emitters using 2D materials *Nano Lett.* **19** 3789–95
[63] Solntsev A S, Agarwal G S and Kivshar Y S 2021 Metasurfaces for quantum photonics *Nat. Photon.* **15** 327–36
[64] Jha P K, Ni X J, Wu C H, Wang Y and Zhang X 2015 Metasurface-enabled remote quantum interference *Phys. Rev. Lett.* **115** 025501
[65] Ma W *et al* 2018 In-plane anisotropic and ultra-low-loss polaritons in a natural van der Waals crystal *Nature* **562** 557–62
[66] Mikhailov S A and Ziegler K 2007 New electromagnetic mode in graphene *Phys. Rev. Lett.* **99** 016803
[67] Bagby J S and Nyquist D P 1987 Dyadic Green's functions for integrated electronic and optical circuits *IEEE Trans. Microwave Theory Tech.* **35** 207–10
[68] Eroglu A 2010 *Wave Propagation and Radiation in Gyrotropic and Anisotropic Media* (Berlin: Springer)
[69] COMSOL Multiphysics 2019 *Version 5.5* (Stockholm: Sweden) http://comsol.com
[70] Fang W and Yang Y P 2020 Directional dipole radiations and long-range quantum entanglement mediated by hyperbolic metasurfaces *Opt. Express* **28** 32599–977
[71] Drezet A 2017 Quantizing polaritons in inhomogeneous dissipative systems *Phys. Rev.* A **95** 023831
[72] Li G X, Li F L and Zhu S Y 2001 Quantum interference between decay channels of a three-level atom in a multilayer dielectric medium *Phys. Rev.* A **64** 013819
[73] Yang Y P, Xu J P, Chen H and Zhu S Y 2008 Quantum interference enhancement with left-handed materials *Phys. Rev. Lett.* **100** 043601
[74] Leong E, Suess R J, Sushkov A B, Drew H D, Murphy T E and Mittendorff M 2017 Terahertz photoresponse of black phosphorus *Opt. Express* **25** 12666–74
[75] Low T, Roldán R, Wang H, Xia F, Avouris P, Moreno L M and Guinea F 2014 Plasmons and screening in monolayer and multilayer black phosphorus *Phys. Rev. Lett.* **113** 106802
[76] Avsar A, Tan J Y, Kurpas M, Gmitra M, Watanabe K, Taniguchi T, Fabian J and Özyilmaz B 2017 Gate-tunable black phosphorus spin valve with nanosecond spin lifetimes *Nat. Phys.* **13** 888–93
[77] Yang B *et al* 2016 Te-doped black phosphorus field-effect transistors *Adv. Mater.* **28** 9408–15
[78] Peres N M R, Guinea F and Castro Neto A H 2006 Electronic properties of disordered two-dimensional carbon *Phys. Rev.* B **73** 125411
[79] Dai S *et al* 2014 Tunable phonon polaritons in atomically thin van der Waals crystals of boron nitride *Science* **343** 1125–9
[80] Wang H, Yuan H, Hong S S, Li Y and Cui Y 2015 Physical and chemical tuning of two-dimensional transition metal dichalcogenides *Chem. Soc. Rev.* **44** 2664–80
[81] Sun Z, Martinez A and Wang F 2016 Optical modulators with 2D layered materials *Nat. Photon.* **10** 227–38
[82] Kuehn S, Hakanson U, Rogobete L and Sandoghdar V 2006 Enhancement of single-molecule fluorescence using a gold nanoparticle as an optical nanoantenna *Phys. Rev. Lett.* **97** 017402
[83] Michalski K A and Nevels R D 2017 On the groundwave excited by a vertical Hertzian dipole over a planar conductor: second-order asymptotic expansion with applications to plasmonics *IEEE Trans. Microwave Theory Tech.* **65** 1133–40